J. Fluid Mech. (1998), *vol.* 355, *pp.* 329–358. Printed in the United Kingdom

Dynamics of interfaces and layers in a stratified turbulent fluid

By N. J. BALMFORTH†, STEFAN G. LLEWELLYN SMITH‡ AND W. R. YOUNG

Scripps Institution of Oceanography, La Jolla, CA 92093-0230, USA

(Received 22 July 1997)

This paper formulates a model of mixing in a stratified and turbulent fluid. The model uses the horizontally averaged vertical buoyancy gradient and the density of turbulent kinetic energy as variables. Heuristic 'mixing-length' arguments lead to a coupled set of parabolic differential equations. A particular form of mechanical forcing is proposed; for certain parameter values the relationship between the buoyancy flux and the buoyancy gradient is non-monotonic and this leads to an instability of equilibria with linear stratification. The instability results in the formation of steps and interfaces in the buoyancy profile. In contrast to previous ones, the model is mathematically well posed and the interfaces have an equilibrium thickness that is much larger than that expected from molecular diffusion.

The turbulent mixing process can take one of three forms depending on the strength of the initial stratification. When the stratification is weak, instability is not present and mixing smoothly homogenizes the buoyancy. At intermediate strengths of stratification, layers and interfaces form rapidly over a substantial interior region bounded by edge layers associated with the fluxless condition of the boundaries. The interior pattern subsequently develops more slowly as interfaces drift together and merge; simultaneously, the edge layers advance inexorably into the interior. Eventually the edge layers meet in the middle and the interior pattern of layers is erased. Any remaining structure subsequently decays smoothly to the homogeneous state. Both the weak and intermediate stratified cases are in agreement with experimental phenomenology. The model predicts a third case, with strong stratification, not yet found experimentally, where the central region is linearly stable and no steps form there. However, the edge layers are unstable; mixing fronts form and then erode into the interior.

1. Introduction

One of the most striking phenomena that occurs in stratified turbulent fluids is the spontaneous formation of mixed layers separated by interfaces. For example, if a fluid with an initially uniform and stable salt gradient is set into turbulent motion by dragging a rod or a grid back and forth, then, as a result of turbulent mixing, the density field evolves into a staircase profile. The salt concentration is almost uniform within the mixed layers, and these are separated by interfaces with steep salt gradients (Linden 1979; Ruddick, McDougall & Turner 1989; Park, Whitehead &

† Permanent address: Department of Theoretical Mechanics, University of Nottingham, Nottingham, NG7 2RD, UK.

‡ Present address: Department of Applied Mathematics and Theoretical Physics, University of Cambridge, Silver Street, Cambridge, CB3 9EW, UK.

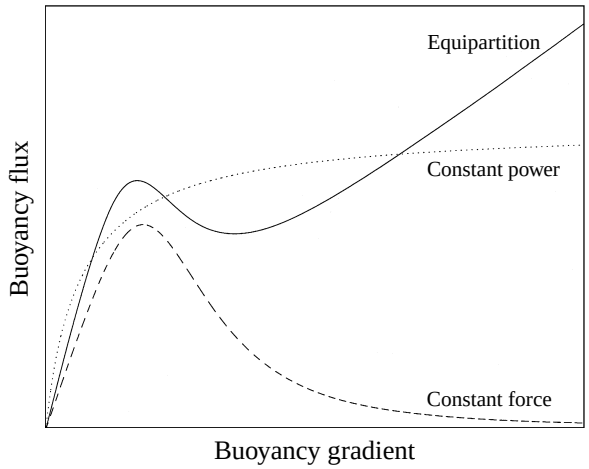

FIGURE 1. A schematic illustration of three possible relations between the buoyancy gradient b_z and the buoyancy flux function, $\mathscr{F}$. The labels on the curves are discussed in § 2.

Gnanadeskian 1994; Holford & Linden 1997*a*, *b*; Rehmann & Koseff 1997). Layer formation has also been experimentally observed in situations in which the turbulent stirring is applied at a boundary; in these cases the layers are extruded into the surrounding non-turbulent fluid (Ivey & Corcos 1982; Thorpe 1982; Browan, Guyomar & Yoon 1987). Other examples of layered stratification involve double-diffusive convective instability and salt fingering (Turner 1973); such structures are observed in the ocean (Schmitt 1994) and in solar ponds (Turner 1985). In more exotic settings, layers are inferred to exist in magma chambers (Chen & Turner 1980) and in stellar interiors (Spiegel 1969).

A key feature of these systems is that the fluid motion is turbulent, and this turbulence is both anisotropic and spatially inhomogeneous (Fincham, Maxworthy & Spedding 1996). The anisotropy is expected because stable stratification suppresses vertical motion. The spatial inhomogeneity of the turbulence is a product of the staircase buoyancy profile: the turbulent kinetic energy is lower in the strongly stable interfaces which separate the mixed layers. In such a situation there is no serious theory of turbulence that one can rely upon and direct numerical simulations cannot access the fully turbulent regime. Instead one must use 'phenomenological' arguments to make progress. In fact, early heuristic arguments by Phillips (1972) and Posmentier (1977) are impressive because they anticipated some aspects of the experiments mentioned above.

Phillips (1972) and Posmentier (1977) argued that the dynamics could be modelled by a nonlinear diffusion equation for $b(z,t)$, the average buoyancy† of the fluid:

$$b_t = \frac{\partial}{\partial z}\mathscr{F}(b_z), \tag{1.1}$$

where $\mathscr{F}$ is the buoyancy flux function. ('Average' or 'mean' represents a horizontal average.) The important feature of the flux function, $\mathscr{F}(b_z)$, introduced by Phillips (1972) and Posmentier (1977) is that it is non-monotonic. In fact, they argued that the flux–gradient relation resembles the curve labelled 'Constant force' in figure 1. With

† We use the Boussinesq approximation and write density perturbations in the fluid in terms of b, the buoyancy: $\rho - \rho_0 \propto b$, where ρ_0 is the density of a reference state.

such a non-monotonic flux–gradient relation, states with spatially uniform buoyancy gradient $g_0 = b_z$ (not to be confused with the gravitational acceleration) are linearly unstable if $\mathscr{F}'(g_0) < 0$. Specifically, if a perturbation locally increases the buoyancy gradient then the buoyancy flux is decreased; thus the buoyancy gradient increases further and so on.

There are two difficulties with such a model, one physical and the other primarily mathematical. The physical problem is that the model has no mechanism to arrest the steepening of the interface. Thus the model predicts an unphysical discontinuous buoyancy profile. Second, the mathematical expression of the layer-forming instability is that the linearized version of (1.1) is a diffusion equation with negative diffusivity. This is a mathematically ill-posed problem, because the growth rate diverges as the wavenumber of the disturbances increases.

To surmount the problem of mathematical ill-posedness, Barenblatt *et al.* (1993) argued that the turbulent flux does not instanteously adjust to the buoyancy gradient. (This effect is to be expected on the basis of an analogy with molecular diffusivity and viscosity; in Maxwell's terminology, the flux has a fading memory of the gradient.) The inclusion of such a delay results in a well-posed mathematical problem (i.e. the growth rate of the linear instability is a bounded function of the wavenumber). However, this extended model still has the property that the model buoyancy field develops discontinuities in a finite time, and this is in disagreement with the experimental result that the interfaces are smooth and have finite thickness (a typical experimental interface thickness is 1 cm, with the steps a factor of five or so larger).

The goal of this paper is to formulate a new model of turbulent mixing in a stably stratified fluid. The model we propose here is based on an explicit consideration of both the mean buoyancy field, $b(z,t)$, and the average density of turbulent kinetic energy, $e(z,t)$. We use dimensional and plausibility arguments to write down two coupled partial differential equations for the evolution of e and b. In order to provide a definite image of the system, we focus on the case in which turbulence is forced by dragging solid objects through a salt-stratified fluid as in the experimental work by Ruddick *et al.* (1989), Park *et al.* (1994), Fincham *et al.* (1996), Holford & Linden (1997*a*, *b*) and Rehmann & Koseff (1997). We assume that this stirring is applied throughout the whole volume of the fluid; the additional complications involved in modelling the horizontal advance of layers into non-turbulent fluid (as seen in the experiments of Ivey & Corcos 1982; Thorpe 1982; Browand *et al.* 1987) are daunting at this stage.

One qualitative difference between our model and earlier proposals is that the flux–gradient relation resembles the curve labelled 'Equipartition' in figure 1. This 'N-shaped' curve has the important feature that there is an intermediate range of buoyancy gradients for which $\mathscr{F}' < 0$ and consequently there is a layer-forming instability, as in the models of Phillips (1972) and Posmentier (1977). But because the flux increases once the gradient becomes sufficiently large, the steepening of the interfaces is arrested. Thus, the equipartition model predicts interfaces with an equilibrium thickness.

A second important difference is that by allowing for the turbulent diffusion of kinetic energy density, the instability is stabilized at high wavenumbers. Thus the model becomes mathematically well-posed.

The details of the model are described further in § 2. Following that, in § 3, we give an account of the layer-forming instability. In § 4, we describe numerical solutions of the model. We discuss the different evolutionary stages of the solution, as well as the parametrical dependences of the system. Sections 5 and 6 contain analytical

considerations largely motivated by the numerical results; these sections are of secondary importance. Finally, § 7 summarizes various predictions of the model and the prospects for testing it against new experiments.

2. The model

Our phenomenological model describes the evolution of average buoyancy $b(z,t)$ (dimensions L/T^2) and average turbulent kinetic energy density $e(z,t)$ (dimensions L^2/T^2) of the fluid. The model is a pair of coupled nonlinear diffusion equations:

$$b_t = (le^{1/2}b_z)_z, \quad e_t = \beta(le^{1/2}e_z)_z - le^{1/2}b_z - \alpha l^{-1}e^{3/2} + \mathscr{P}, \tag{2.1a,b}$$

where l is the mixing length of the turbulence (to be prescribed shortly) and α and β are dimensionless constants. The various terms are rationalized as follows. Both the buoyancy field and kinetic energy density are transported by turbulent eddy diffusion and on dimensional grounds the eddy diffusivities are both proportional to $le^{1/2}$. By taking $\beta \neq 1$, we allow for the possibility that turbulent kinetic energy and buoyancy do not diffuse at the same rate (however, in what follows, we will mainly consider the case $\beta = 1$). The term $-le^{1/2}b_z$ in the energy equation is needed to account for the decrease in e which accompanies vertical mixing of the stable stratification by the turbulence (the conversion of kinetic to potential energy; see (2.2) below). The term $-\alpha l^{-1}e^{3/2}$ is the dissipation of turbulent kinetic energy; after Kolmogorov this term is conventionally denoted by ε. Again, on dimensional grounds, this form for ε is required if one can use only e and l to construct the relevant quantity. Finally, $\mathscr{P}$, the energy production term, expresses the manner in which the stirring device excites the turbulent motion, and will be discussed below.

As boundary conditions, we impose $b_z = e_z = 0$ at the bottom and top of the fluid, $z = 0$ and $z = H$, where H is the depth of the fluid. This ensures that energy and buoyancy are not fluxed into the system and that the evolution of the total energy is effected only by dissipation and forcing. In fact, the global energy balance of the system is

$$\frac{\mathrm{d}}{\mathrm{d}t}\int_0^H (e - zb)\,\mathrm{d}z = \int_0^H (\mathscr{P} - \alpha l^{-1}e^{3/2})\,\mathrm{d}z. \tag{2.2}$$

In forming this global balance equation, the term $-le^{1/2}b_z$ in the kinetic energy equation cancels with a term which comes from the buoyancy equation. This is the exchange between kinetic and potential energy which accompanies turbulent buoyancy mixing.

2.1. *The mixing length*

The model employs a mixing length scale, l. For the stirred unstratified fluid, there is a natural estimate for the mixing length, namely a length d which is proportional to some characteristic dimension of the stirring device. This prescription is not correct when the stratification is strong because there is then a substantial suppression of vertical motion, in which case $l \ll d$. In this limit, the mean kinetic energy and mean buoyancy suggest an alternative characteristic length scale, $l \propto (e/b_z)^{1/2}$ (see also figure 12 of Park *et al.* 1994). As a simple model we take

$$\frac{1}{l^2} = \frac{1}{d^2} + \gamma\frac{b_z}{e}, \tag{2.3}$$

	$\mathscr{P}$	f_0	e_0
Constant power	W	$\dfrac{W}{1+\alpha\gamma}$	$\dfrac{W\gamma^{1/2}}{(1+\alpha\gamma)g_0^{1/2}}$
Constant force	$\mathscr{Z}e^{1/2}$	$\dfrac{\gamma^{1/2}\mathscr{Z}^2}{(1+\alpha\gamma)^2 g_0^{1/2}}$	$\dfrac{\gamma\mathscr{Z}^2}{(1+\alpha\gamma)^2 g_0}$
Equipartition	$\alpha U^2 e^{1/2}/l$	$\dfrac{\alpha U^2(\gamma g_0)^{1/2}}{1+\alpha\gamma}$	$\dfrac{\alpha\gamma U^2}{1+\alpha\gamma}$.

TABLE 1. Three models of the energy production term $\mathscr{P}$, along with the values of buoyancy flux, f_0, and equilibrium energy, e_0, in the limit of asymptotically large buoyancy gradients, g_0. Notice how the dependence of the flux f_0 on the gradient g_0 differs in the three cases (cf. the behaviour of the three curves in figure 1 when the buoyancy gradient is large)

or equivalently,

$$l = \frac{de^{1/2}}{(e+\gamma d^2 b_z)^{1/2}}, \tag{2.4}$$

so that l interpolates between the two limits, d and $(e/b_z)^{1/2}$, described above. The non-dimensional mixing-length parameter, γ, becomes important in the strongly stratified limit: $l \approx (e/\gamma b_z)^{1/2}$.

The prescription above for l is related to Ozmidov's length, which is defined by $l_O = (\varepsilon/N^3)^{1/2}$, where $N^2 = b_z$ is the buoyancy frequency. In the strongly stratified limit, and using $\varepsilon = -\alpha l^{-1} e^{3/2}$, both l_O and the our mixing length l are proportional to $(e/b_z)^{1/2}$.

2.2. *Energy production*

The form of the production term, $\mathscr{P}$, is the crux of the present approach. To fully appreciate the issues here it is instructive to consider the three possible forms for $\mathscr{P}$ shown in table 1. The simplest hypothesis is that the forcing delivers constant power per unit mass, W (dimensions L^2/T^3), to the fluid. Alternatively, one can suppose that the forcing exerts a constant force per unit mass, $\mathscr{Z}$ (dimensions L/T^2). The third possibility, and the one we which we adopt, is that the eddy speed, $e^{1/2}$, adjusts to a velocity scale, U (dimensions L/T), which is proportional to the speed of the stirring device, on the eddy turnover timescale, $l/e^{1/2}$. Hence, we take the energy input to have the form $\alpha e^{1/2} U^2/l$.

Our physical motivation for this choice is as follows. As the stirring device moves though the fluid, it excites motion by generating a wake and also, perhaps, by radiating internal gravity waves. But in the experiments of Ruddick *et al.* (1989) and Park *et al.* (1994) the generation of internal waves is not very efficient because the rod is perpendicular to the density surfaces and the direction of motion is horizontal. Consequently, we discard waves as a significant source of the fluid turbulence and attribute that motion mainly to the breakdown of the wake. Typical fluid velocities in this wake are comparable to the speed of the stirring device, U, and the timescale for breakdown is of order the eddy turnover time, $l/e^{1/2}$.

With this prescription for the third model, the kinetic energy equation (2.1*b*) becomes

$$e_t = \beta(le^{1/2}e_z)_z - le^{1/2}b_z + \alpha(e^{1/2}/l)(U^2 - e). \tag{2.5}$$

Notice that the non-dimensional parameter α determines the rapidity of the relaxation of e to U^2. We refer to this third model in table 1 as 'equipartition' because, in the absence of stratification, the turbulent kinetic energy level adjusts to that of the stirring device (this appellation is not meant to suggest a connection with thermodynamics, nor with statistical mechanical theories of turbulence).

Once one has adopted a model for $\mathscr{P}$ then it is straightforward to obtain the flux–gradient relation by looking for a steady solution of (2.1a, b) with $(e, b) = (e_0, g_0 z)$, where e_0 and g_0 are constants. The buoyancy equation (2.1a) is automatically satisfied for such spatially homogeneous states and the energy balance (2.1b) becomes

$$\mathscr{P} = l_0 {e_0}^{1/2} g_0 + \alpha l_0^{-1} e_0^{3/2}, \tag{2.6}$$

which determines the equilibrium turbulent kinetic energy density, e_0, as a function of the buoyancy gradient g_0. The buoyancy flux associated with this spatially uniform basic state is then $f_0 = l_0 {e_0}^{1/2} g_0$. The three different choices for $\mathscr{P}$ in table 1 lead to the three different flux–gradient relations shown in figure 1.

The different cases in figure 1 are distinguished by the behaviour of e_0 and f_0 when the buoyancy gradient g_0 is large. In this strongly stratified limit the mixing length is given by $l_0 \approx (e_0/\gamma g_0)^{1/2}$ and the energy equation (2.1b) implies that $(1 + \gamma\alpha) e_0 (g_0/\gamma)^{1/2} \approx \mathscr{P}$. Thus, the buoyancy flux is

$$f_0 \approx \frac{\mathscr{P}}{1 + \alpha\gamma} \qquad \text{(if } g_0 \text{ is large)}. \tag{2.7}$$

Next, given the different forms for $\mathscr{P}$ one can obtain the equilibrium kinetic energy density and, finally, the flux–gradient relation. The results are summarized in table 1.

The constant-power assumption results in a flux which asymptotes to a maximum value when the buoyancy gradient g_0 is large. In this case, the buoyancy flux increases monotonically for all values of g_0, and so there is no layering instability. With the constant-force assumption, the thickness of the interfaces becomes zero in a finite time. Thus the first two models in table 1 are incapable of explaining the experimental results. The equipartition model has the N-shaped flux–gradient relation in figure 1. A layering instability is possible because there is a range of buoyancy gradients within which the flux decreases as the gradient increases. But because the buoyancy flux increases when b_z is large, the thickness of the interfaces cannot decrease indefinitely. Thus, the equipartition model has an equilibrium step thickness.

Of course, if one includes the effects of molecular diffusivity by adding the term $D_{\mathrm{mol}} b_{zz}$ to the right-hand side of (2.1a), all three curves in figure 1 will eventually rise at extremely large values of the buoyancy gradient (although in the constant-power case the flux–gradient relation remains monotonic). However, the step thickness in the experiments of Ruddick *et al.* (1989) and Park *et al.* (1994) is at least 1 cm and the molecular diffusion time of salt through this distance is many hours; this is too long relative to the eddy turnover time to be important. Thus we argue that there is a turbulent mechanical process which results in a rise of the flux–gradient curve before molecular processes become important (see also Ruddick *et al.* 1989). The equipartition model implicitly assumes a mechanical process of this sort, and produces the $f_0 \propto g_0^{1/2}$ dependence in table 1.

Our model also does not include direct molecular dissipation of turbulent kinetic energy. Consequently, when we come to non-dimensionalize in the next subsection, there is no parameter equivalent to the Reynolds number. One way of incorporating

this additional physics is to add a term, $-ve/l^2$, to the right-hand side of (2.1*b*). Given the many rough ingredients in the model, we do not pursue this embellishment.

2.3. *Non-dimensional form*

Finally, we can non-dimensionalize the equations. It is convenient to use the buoyancy gradient, $g \equiv b_z$, as a dependent variable and make the following definitions of dimensionless quantities:

$$\hat{t} = Ut/\gamma d, \quad \hat{z} = z/\gamma^{1/2}d, \quad \hat{e} = e/U^2, \quad \hat{g} = \gamma d^2 g/U^2, \quad \hat{l} = l/d. \tag{2.8}$$

The resulting system of non-dimensional equations is then

$$g_t = (le^{1/2}g)_{zz}, \tag{2.9a}$$

$$e_t = \beta(le^{1/2}e_z)_z - le^{1/2}g + \epsilon l^{-1}(1-e)e^{1/2}, \tag{2.9b}$$

$$l = \frac{e^{1/2}}{(e+g)^{1/2}}, \tag{2.9c}$$

where $\epsilon \equiv \alpha\gamma$ and we have lightened notation by dropping the hats. The boundary conditions are $g = e_z = 0$ at $z = 0$ and $z = H$. This set of equations resembles a model of stratified turbulent mixing formulated by Barenblatt (1983). Barenblatt considered unforced evolution, so that his model has no energy production term analogous to the penultimate term, $\epsilon l^{-1}e^{1/2}$, in (2.9*b*), and he employed a very different prescription for the mixing length l.

3. Equilibria and their stability

We now consider equilibrium solutions of (2.9*a–c*) and examine their stability. With no-flux boundary conditions on b and e the system runs down to the trivial solution $(g, e) = (0, 1)$. Hence the ultimate equilibrium is uniform density with equipartition. To avoid this trivial equilibrium, we relax the boundary conditions and consider solutions which are independent of z with uniform 'basic state' values g_0 and e_0. These pseudo-equilibria prove useful later in understanding the layer formation process.

For such equilibria, equation (2.9*b*) becomes

$$e_0 = \tfrac{1}{2}\left\{1 - g_0(1+r) + \left([1-g_0(1+r)]^2 + 4g_0\right)^{1/2}\right\} \equiv \mathscr{E}(g_0), \tag{3.1}$$

where $r \equiv 1/\epsilon$. If $g_0 = 0$, then (3.1) reduces to equipartition, $e_0 = 1$. Figure 2 shows e_0 as a function of g_0 for various values of r. Given e_0 and g_0, the flux of buoyancy is then

$$f_0 = \frac{\mathscr{E}(g_0)g_0}{(\mathscr{E}(g_0)+g_0)^{1/2}} \equiv \mathscr{F}(g_0). \tag{3.2}$$

We refer to the the function $\mathscr{F}$ as the 'equilibrium flux–gradient relation' (see figure 3).

The stability of these equilibria can be assessed by linearizing (2.9*a, b*) about the base state, (g_0, e_0), and looking for exponentially growing solutions. We rewrite (2.9*a, b*) in the form

$$g_t = f_{zz}, \quad e_t = (\kappa e_z)_z + p, \tag{3.3a, b}$$

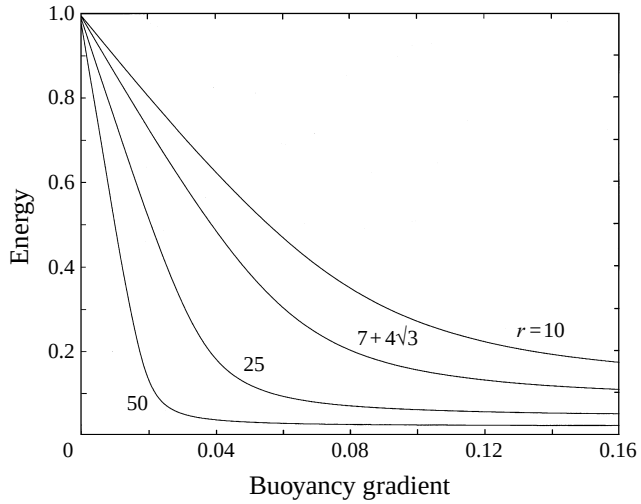

FIGURE 2. Equilibrium energy, $\mathscr{E}(g_0)$, against buoyancy gradient, g_0, for $r = 10$, 25, $7 + 4\sqrt{3}$ and 50. When g_0 is large, $\mathscr{E} \sim 1/(1 + r)$. Note that $r \equiv 1/\epsilon$.

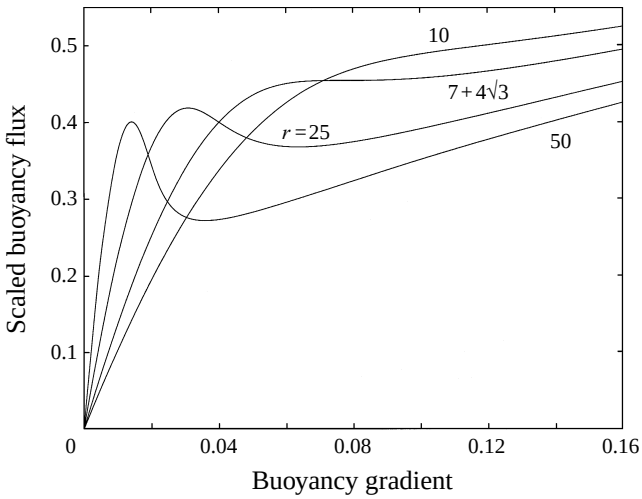

FIGURE 3. Scaled buoyancy flux, $\mathscr{F}(g_0)/(1 + r)$, against buoyancy gradient, g, for $r = 10$, $7 + 4\sqrt{3}$, 25 and 50. The curve with $r = 7 + 4\sqrt{3}$ has a higher-order stationary point ($\mathscr{F}'' = \mathscr{F}' = 0$) at $g_0 = 1/\sqrt{3} - 1/2$.

where

$$f \equiv eg/(e + g)^{1/2}, \tag{3.4a}$$

$$p \equiv \epsilon(e + g)^{1/2}(1 - e) - eg/(e + g)^{1/2}, \tag{3.4b}$$

$$\kappa \equiv \beta e/(e + g)^{1/2}. \tag{3.4c}$$

The equilibrium solution satisfies

$$p(g_0, e_0) = 0 \qquad \text{and} \qquad f(g_0, e_0) = f_0. \tag{3.5}$$

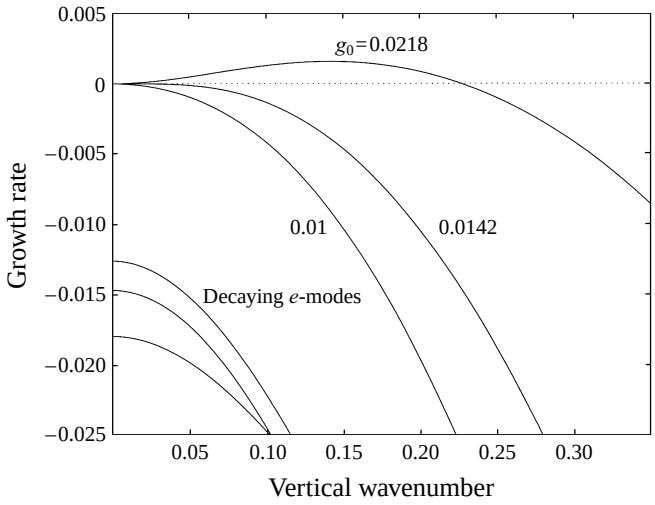

FIGURE 4. Growth rate, s, against the vertical wavenumber, m, for $r = 50$. In the case with $g_0 \approx 0.0142$, the buoyancy mode is marginally stable; that is, $\mathscr{F}' = 0$.

Thus we have a one parameter, g_0, family of solutions. From (3.5) it follows that

$$\mathscr{F}'(g_0) = (p_e f_g - p_g f_e)/p_e, \tag{3.6}$$

where the various partial derivatives, p_e and so on, are evaluated at (g_0, e_0), and $e_0 = \mathscr{E}(g_0)$.

Next, we pose the solutions $g = g_0 + g_1 \exp(st + \mathrm{i}mz)$ and $e = e_0 + e_1 \exp(st + \mathrm{i}mz)$. The linear problem for the perturbations, g_1 and e_1, is

$$s \begin{pmatrix} g_1 \\ e_1 \end{pmatrix} = \begin{pmatrix} -m^2 f_g & -m^2 f_e \\ p_g & -m^2\kappa + p_e \end{pmatrix} \begin{pmatrix} g_1 \\ e_1 \end{pmatrix}, \tag{3.7}$$

which determines the growth rate s as a function of the wavenumber m. Figure 4 shows some examples of the dispersion relation.

There are two modes which we can classify by examining the behaviour at $m = 0$. One mode has eigenvalue $s \approx p_e$ near $m = 0$. But, provided the buoyancy gradient is positive (the fluid is stably stratified), it is straightforward to show that $p_e < 0$. As a result, this mode is always stable. The associated eigenvector of this mode takes the form $(g_1, e_1) = (0, 1)$ for $m \to 0$. Hence we use the designation 'energy mode'.

The second mode in figure 4 is a 'buoyancy mode'; depending on the values of g_0 and ϵ, this mode can be unstable. However, as figure 4 shows, the instability has a high-wavenumber cutoff, and so, in contrast to model (1.1), the mathematical problem here is well-posed. Near $m = 0$, the buoyancy mode takes the form

$$(g_1, e_1) \approx (1, -p_g/p_e), \qquad s \approx -\mathscr{F}' m^2. \tag{3.8}$$

Hence the buoyancy mode is unstable if $\mathscr{F}'(g_0) < 0$; this is the result of Phillips (1972) and Posmentier (1977).

The high-wavenumber cutoff, m_*, is given by

$$m_*^2 = \kappa^{-1} f_g^{-1} \left(p_e f_g - p_g f_e\right) = \kappa^{-1} f_g^{-1} p_e \mathscr{F}'. \tag{3.9}$$

This result shows that diffusion of turbulent kinetic energy (that is, $\kappa \neq 0$) is essential for the high-wavenumber cutoff.

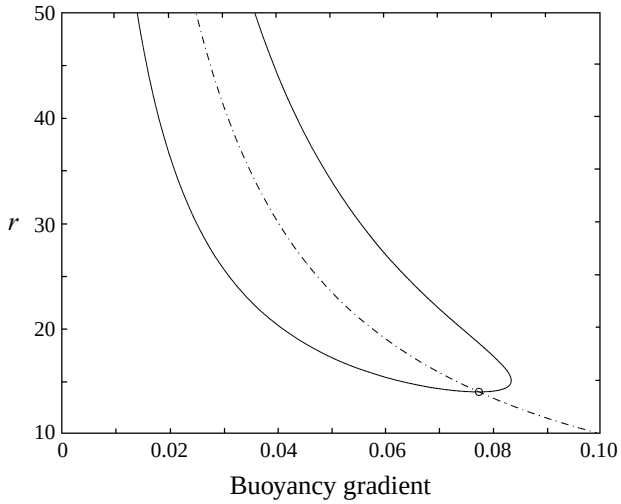

FIGURE 5. The solid curve is the locus on which $\mathscr{F}'(g_0) = 0$. Inside the solid curve, $\mathscr{F}' < 0$, and the buoyancy mode is unstable (see (3.8)). The dashed curve is the locus on which $\mathscr{F}''(g_0) = 0$. The small circle corresponds to the intersection of these loci and is the critical point in the amplitude expansion of the Appendix. The critical point is given by $(g, r) = (1/\sqrt{3} - 1/2, 7 + 4\sqrt{3})$.

Finally, we display the unstable region of the (g_0, r) parameter plane by plotting the curve along which $\mathscr{F}'(g_0) = 0$: see figure 5. Provided that r is greater than a critical value, r_c, there is a range of unstable buoyancy gradients limited by the two values of g_0 for which $\mathscr{F}' = 0$. The disappearance of the unstable range of buoyancy gradients corresponds to the merging of the two extrema of $\mathscr{F}'(g_0)$ at a higher-order stationary point with $\mathscr{F}' = \mathscr{F}'' = 0$. An explicit calculation shows that $r_c = 7 + 4\sqrt{3}$ and the corresponding value of g_0 is $g_{0c} = (2 - \sqrt{3})/2\sqrt{3}$.

4. Numerical solutions

We now solve equations (2.9*a*) and (2.9*b*) numerically, using a finite element collocation procedure designed to solve coupled nonlinear parabolic partial differential equations (Keast & Muir 1991). The spatial resolution employed (typically 4 000 polynomial interpolants over the domain) is more than sufficient to resolve the sharp features that develop in the numerical simulations.

As initial conditions, we take

$$g = g_i \left\{ 1 - \frac{\cosh\left[20(z/H - 1/2)\right]}{\cosh 10} \right\}, \quad e = e_i. \tag{4.1a,b}$$

These initial conditions provide two more parameters, namely an initial buoyancy gradient, g_i, and a background kinetic energy density, e_i. The important feature of the initial condition is that over an extensive region inside the domain the buoyancy gradient and kinetic energy are close to an equilibrium of the kind discussed in the last section. However, such an equilibrium does not satisfy the boundary condition, $g = 0$ at $z = 0$ and H. In (4.1*a*), this is repaired in edge regions that together occupy about a fifth of the domain. If $e_i \approx 0$, then the initial conditions (4.1*a, b*) are arguably the closest approximation to the initial state of the experiments of Ruddick *et al.* (1989) and Park *et al.* (1994).

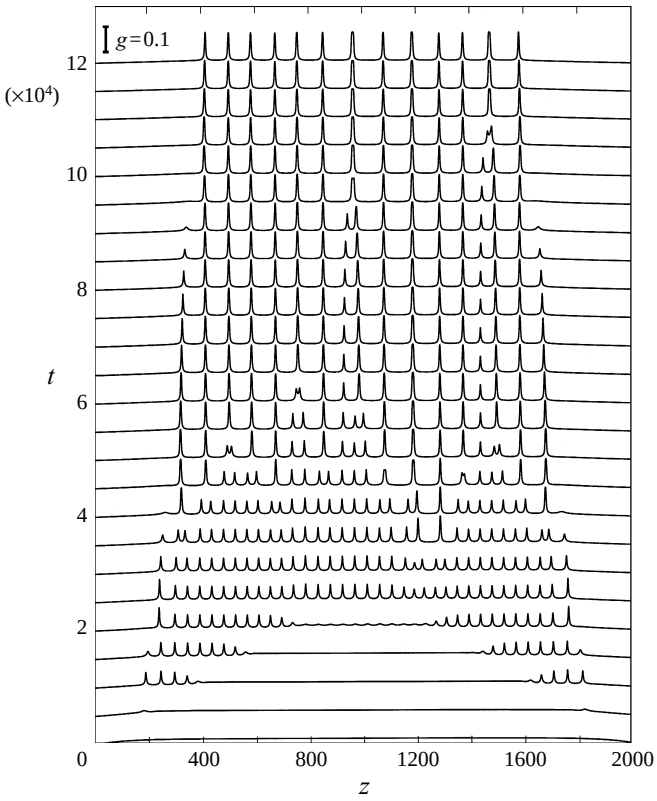

FIGURE 6. Profiles of the buoyancy gradient, g, as a function of z for different values of t. The vertical axis is time, and the profiles are spaced at time intervals of 5000. The thick bar at the top left-hand corner gives the amplitude scale for g.

In their experiments, Park *et al.* (1994) defined a Richardson number

$$Ri = \frac{N_i^2 d_*^2}{U_*^2}, \tag{4.2}$$

where d_* and U_* denote the actual diameter and speed of the stirring rod. N_i^2 is the dimensional initial buoyancy gradient in the centre of the tank. Then, from (2.8), $g_i = \gamma d^2 N_i^2 / U^2$, and so

$$Ri = \frac{1}{\gamma}\left(\frac{U}{U_*}\right)^2 \left(\frac{d_*}{d}\right)^2 g_i \tag{4.3}$$

(in general, the lengths d and d_*, and speeds U and U_* will not be the same). Hence, g_i in (4.1*a*) is proportional to the experimental Richardson number.

4.1. *Step formation and evolution*

In figures 6 to 8 we show details of a numerical solution using the initial condition (4.1*a*, *b*) with $g_i = 0.0218$ and $e_i = 0.0994$, at the parameter values, $r = 1/\epsilon = 50$ and $\beta = 1$. The domain is $0 < z < H = 2000$. The value of r is well above the critical value r_c for which instability appears, and the initial buoyancy gradient g_i is in the middle of the unstable range (figure 5). The initial kinetic energy density e_i lies close to $\mathscr{E}(g_i)$, where $\mathscr{E}(g)$ is defined in (3.1).

Figure 6 shows a succession of snapshots of the buoyancy gradient. Figure 7

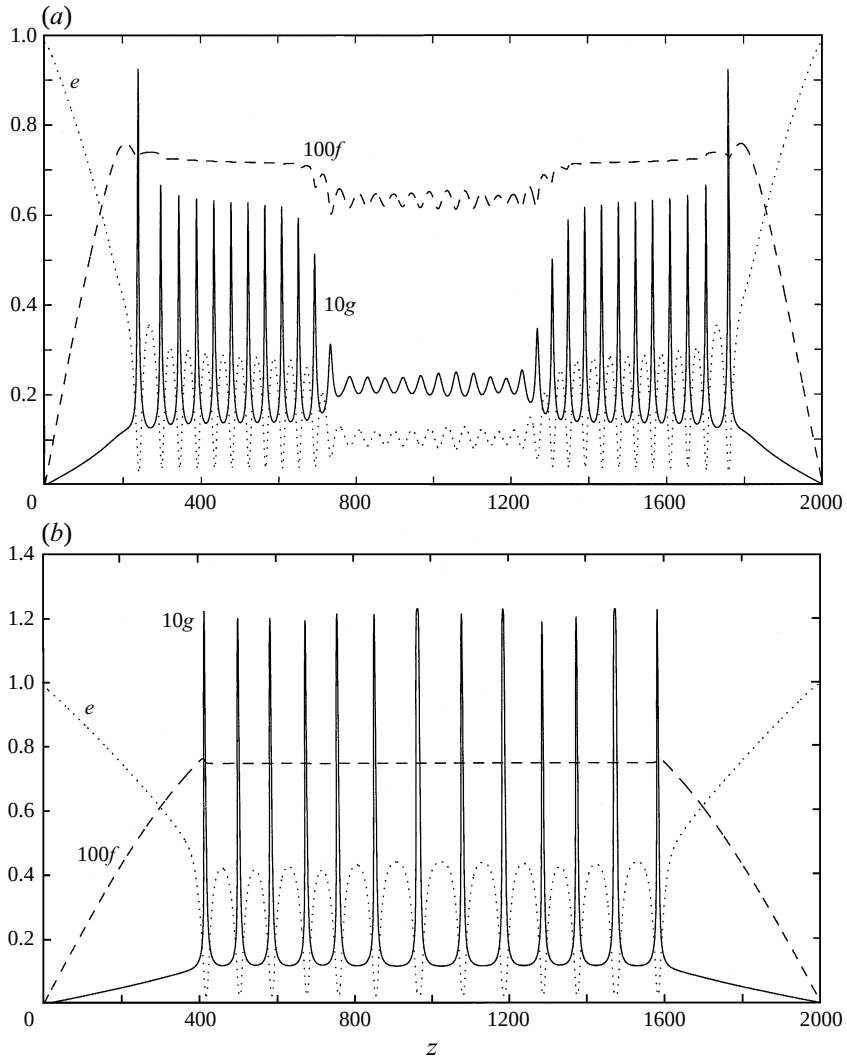

FIGURE 7. Kinetic energy density, e, scaled buoyancy gradient, $10g$, and scaled buoyancy flux $100f$ at two different values of time: (*a*) $t = 20\,000$, (*b*) $t = 120\,000$. At the larger time value, the flux is constant outside the 'edge layers' and roughly linear inside them. The left-hand edge layer in (*b*) is the region $0 < z < 400$.

shows the buoyancy gradient, g, kinetic energy, e, and buoyancy flux, f, at two instants. Finally, figure 8 shows the evolving buoyancy flux as a surface plot above the (z, t)-plane.

The evolution can be roughly divided into three stages. The first features to emerge are related to the linear instability of the equilibrium state. This instability initially appears at the borders between the central region (in which g is uniform) and the boundary regions (in which g decreases to zero at $z = 0$ and $z = H$). This is because the border is where the linearly unstable g_i in the central region has the largest initial perturbation. The instability appears next in the centre of the domain (see figure 7*a*). The progression from the edge to the centre in figure 6 gives the mistaken impression that the instability moves inwards from the edges. However, the unstable disturbances

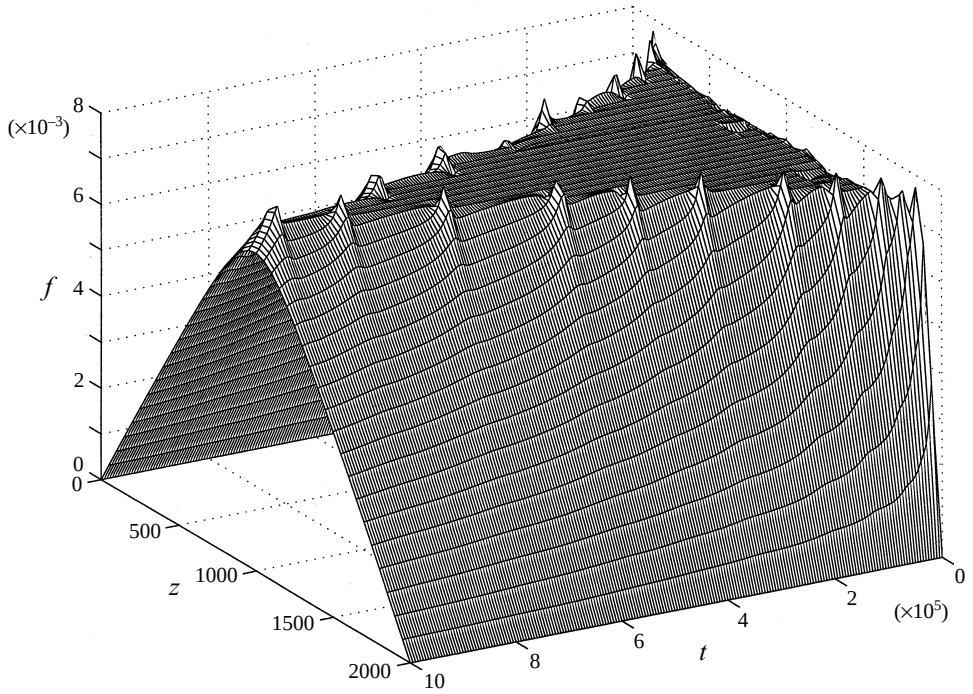

FIGURE 8. Surface plot of the buoyancy flux f as a function of z and t. The initial evolution of f is hidden in this plot. The state of constant flux, which is characteristic of the slow evolution of the central layers, is the triangular plateau. In the text, we refer to the constant value of f on the plateau as f_*.

are simply growing in place. (This feature of the initial evolution is also apparent in the experiments of Holford & Linden 1997*a*.)

Thus, in this first evolutionary stage, the instability creates a sequence of 'spikes' in the buoyancy gradient or, equivalently, steps in the buoyancy profile.

The second evolutionary stage, from $t \approx 30\,000$ on, consists of a much slower development of the pattern of gradient spikes. This 'metastable pattern' slowly changes as a result of interfaces gradually being eroded away from the periphery of the pattern, and by internal layer interactions (figure 6). The internal layer interactions lead to spikes drifting together and merging. Two merging events are displayed further in figure 9.

The final evolutionary stage emerges once all the interfaces in the central pattern have been destroyed by the expansion of the edges: the centre cannot hold. This leaves a smooth, triangular distribution of the buoyancy flux (see figure 8) that decays slowly to the ultimate homogenized state.

This three-stage evolution is very similar to that observed experimentally. In fact, the pattern shown in figure 6 bears many similarities to figure 10 of Park *et al.* (1994). Another interesting point of comparison is in the buoyancy flux. A striking feature of the second evolutionary stage is that the spike pattern evolves at almost constant buoyancy flux in the interior of the domain (figure 8). In a sense, this is simply a consequence of the slow evolution of the second phase: in order to achieve a slowly evolving state, equation (2.9*a*) requires that the flux be uniform. In fact, the residual variations in the flux are correlated with the merging or decay of layers (figures 8

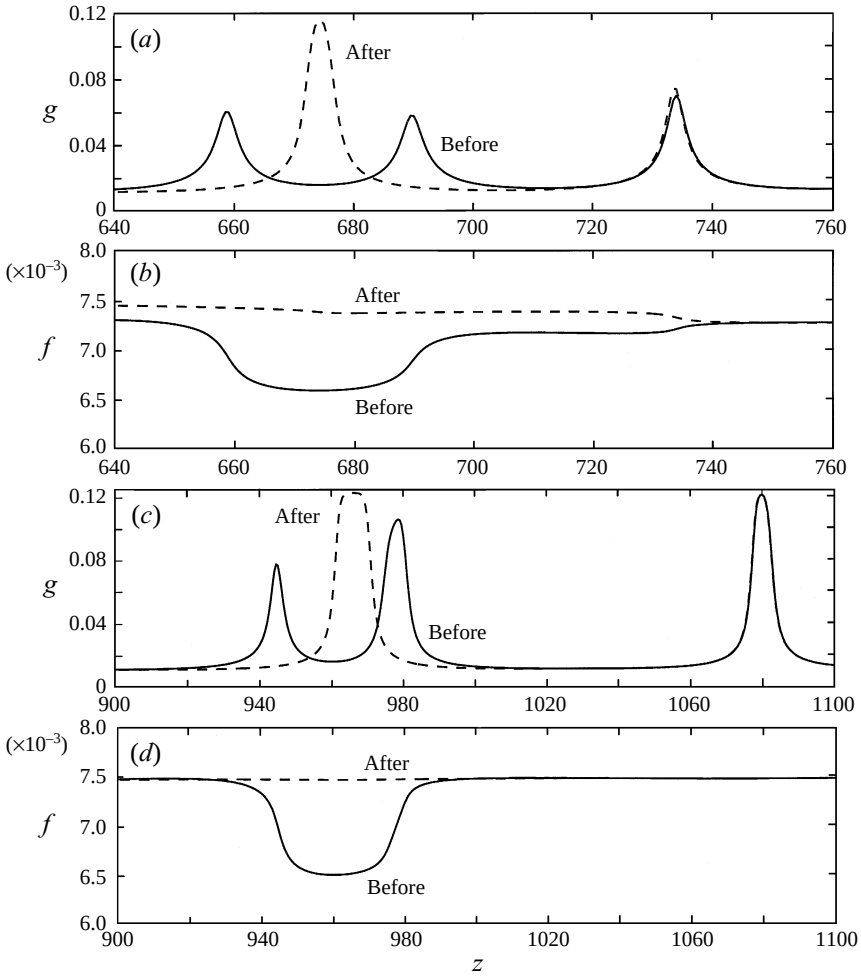

FIGURE 9. Buoyancy gradient (a, c) and (b, d) during two merger events. (a, b) $t = 40\,000, 50\,000$; (c, d) $t = 90\,000, 100\,000$. Note the different spatial scales.

and 9). These features of the flux closely correspond to the experimental data in figures 16 and 17 of Park *et al.* (1994).

We may define a mixing efficiency (or flux Richardson number), R_f, by

$$R_f(t) \equiv \frac{\displaystyle\int_0^H f \, \mathrm{d}z}{\displaystyle\int_0^H \mathscr{P} \, \mathrm{d}z} = \frac{\displaystyle\int_0^H eg(e+g)^{-1/2} \, \mathrm{d}z}{\epsilon \displaystyle\int_0^H (e+g)^{1/2} \, \mathrm{d}z}. \tag{4.4}$$

This non-dimensional parameter relates the integrated buoyancy flux to the integrated power input to the system, and is hence a natural measure of the efficiency of the turbulent energy input in redistributing the buoyancy in the system. Figure 10 shows the evolution of R_f as a function of time. The measured values of R_f of Park *et al.* (1994) lie in the range 0.02–0.12. While the present theory predicts values that are a little high in comparison, no attempt was made to adjust parameters to make the two coincide. In particular, varying ϵ would almost certainly lead to a better comparison.

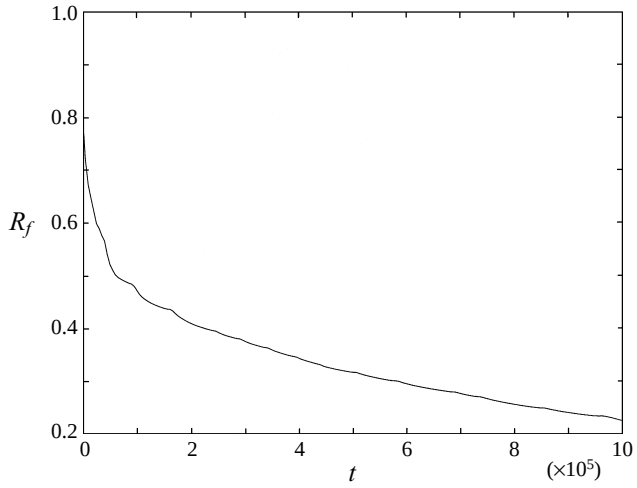

FIGURE 10. Mixing efficiency, R_f, as a function of time.

A more precise calibration of ϵ in this fashion was not attempted given the crudity of the model.

4.2. *Layer dynamics in the central region*

The layers shown in figure 6 are created through the instability of the initial condition. As a result, the initial evolution is typically dominated by the growth of the most unstable mode. This suggests that the number of spikes correlates roughly with the number of wavelengths of this mode that fit into the central region (4/5 of the domain). This expectation is supported by the numerical calculations. For example, in figure 6, the most unstable mode fits about 36 wavelengths into the central region of the simulations, and there are 36 identifiable spikes.

To show more details of the subsequent evolution of the gradient spikes we isolate the peak of each spike and follow it in space and time; that is, we plot the world lines of the spikes. In figure 11 we show the world lines of the spikes for the solution in figures 6 to 8. This picture shows both the gradual coarsening of the central pattern which results from binary mergers, and the simultaneous erosion by the inexorable expansion of the edge layers.

The coarsening dynamics revealed in figure 11 is remarkably similar to the reduced descriptions of the dynamics of fronts or kinks in theories of phase separation (Bates & Xun 1995; Kawasaki & Ohta 1982; Fraerman *et al.* 1997). In fact, this connection is more than qualitative: in the vicinity of the critical point of figure 5, we can use asymptotic methods to reduce the system (3.3) to the Cahn–Hilliard equation (Cahn & Hilliard 1958), a widely used model of phase separation. The calculation is summarized in the Appendix. Thus there are also mathematical reasons why we might expect the similarity.

A key feature of the layer dynamics is that throughout the interactions the buoyancy flux, f, remains constant in the interior of the domain (see figure 8). This provides the basis of the analytical approach we follow in the next section to understand some properties of the spike pattern. In addition, because g is conserved in layer

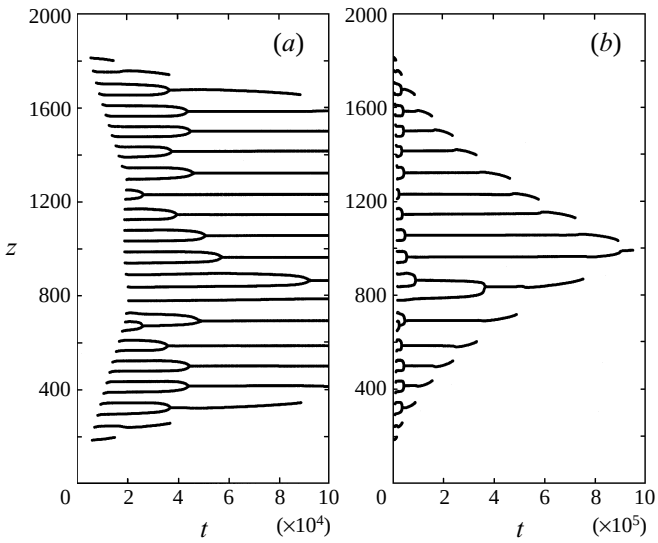

FIGURE 11. Space–time diagram showing the spikes in g over a threshold amplitude of $1.5g_i$. The two panels have different time resolution: (*a*) short time, (*b*) long time.

interactions, then it must be the case that merging events preserve the integral

$$\int_{z_1}^{z_2} g(z,t)\,\mathrm{d}z = b(z_2,t) - b(z_1,t), \tag{4.5}$$

where z_2 and z_1 indicate two levels above and below the merging layers. In other words, the merger preserves constant area under the curve $g(z,t)$, which is just the total change in buoyancy between z_1 and z_2. This is evident in figure 6 at early times, and in 9 (*a*), where two small spikes tend to merge into one with approximately twice the height. This builds spikes with peak amplitudes in the vicinity of 0.11. Somewhat later in figure 6, the gradient spikes no longer build in amplitude when they merge. In fact, they reach a peak amplitude beyond which they do not go (the maximum amplitude is about 0.123; see figure 9 *c*). Instead, in order to preserve the area, the new gradient spike is thicker than its predecessors.

The maximum spike amplitude ($g \approx 0.123$) is related to the special, constant value of the flux reached in the interior of the domain. This value is $f_* = 0.0075$ for the simulation in figure 8. Figure 12 shows how the value of f_* can be used to determine both the maximum and minimum value of the gradient g by exploiting the equilibrium flux–gradient relation.

4.3. *Dependence on initial condition*

The solution presented in figures 6 to 8 illustrates the typical features of the creation and evolution of layers from the initial condition (4.1). However, such behaviour is also a characteristic of much more general classes of initial conditions. One reason for this common behaviour is that the evolution is insensitive to the initial value of the kinetic energy, e_i. This arises because of the strongly damped nature of the 'energy mode' in figure 4. At the start of the evolution the energy relaxes rapidly to the local equilibrium determined by the buoyancy gradient; that is, to $\mathscr{E}(g)$ in (3.1). Hence, the details of the initial value of e are quickly erased and the original buoyancy profile becomes all important.

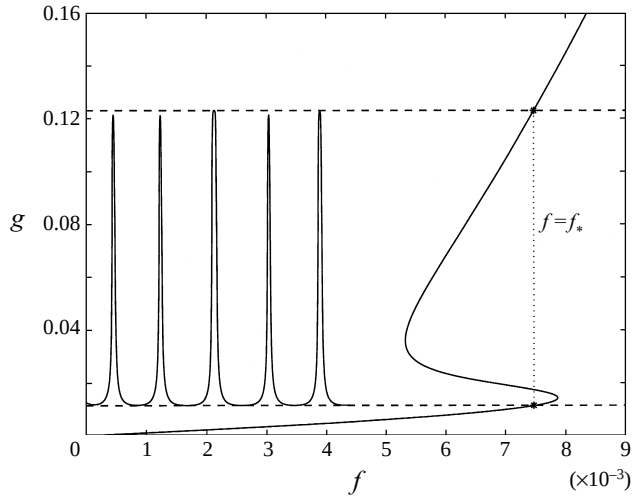

FIGURE 12. The solid, S-shaped curve shows the equilibrium flux–gradient relation, $\mathscr{F}(g)$. In this figure the gradient g is the vertical axis. From the numerical solution we find that the buoyancy flux in the central region is very nearly uniform and equal to $f_* = 0.0075$. The dotted line, $f = f_*$, connects the maximum gradient at the top of the spikes to the minimum gradient at the bottom of the spikes. That is to say, the peak-to-trough excursion of the spikes in g connects the two stable equilibrium gradients corresponding to f_*. This connection is illustrated by the curve to the left which shows the buoyancy gradient over part of the domain at $t = 195\,000$ (with a scaled horizontal axis).

Given that the initial buoyancy gradient exerts a key influence on the subsequent evolution, we have systematically explored the dependence on g_i (equivalently, the Richardson number in (4.3)). Broadly speaking, there are three behavioural regimes that the system can fall into. The distinction between the three regimes is simply whether g_i in (4.1*a*) is to the left of the unstable region in figure 5, within the unstable region, or to the right of the unstable region.

First, if g_i is small, the system is to the left of the unstable region in figure 5. In this case there is no layering instability anywhere in the domain and the initial buoyancy gradient diffuses away while the energy approaches the equipartition value. This behaviour is in accord with experiment. The dimensional buoyancy gradient is given by $g_i U^2/\gamma d^2$. So at fixed values of the dimensional buoyancy gradient, small values of g_i are obtained by making U/d large: that is, by stirring vigorously. This is in agreement with Ruddick *et al.* (1989) and Park *et al.* (1994), who found that for vigorous stirring (large U) interfaces do not form.

Second, for larger values of g_i, the interior of the domain becomes unstable. That is, g_i is within the unstable region in figure 5. This is the behaviour we have already described and illustrated in figures 6–12. As another example of this regime consider figure 13. This solution shows the buoyancy gradient evolving from an initial condition with a less regular spatial structure than that of (4.1*a*). But, on average, the initial gradient is within the unstable region. In this case, just as before, gradient spikes form, then subsequently merge and decay. The main qualitative difference from the results portrayed earlier is that the spikes emerge quickly all over the interior of the domain. Moreover, they almost immediately reach the final amplitude of 0.12 without forming an intermediate set of roughly half the amplitude. The spikes often emerge from where the initial condition has largest gradient, but this is not always the case.

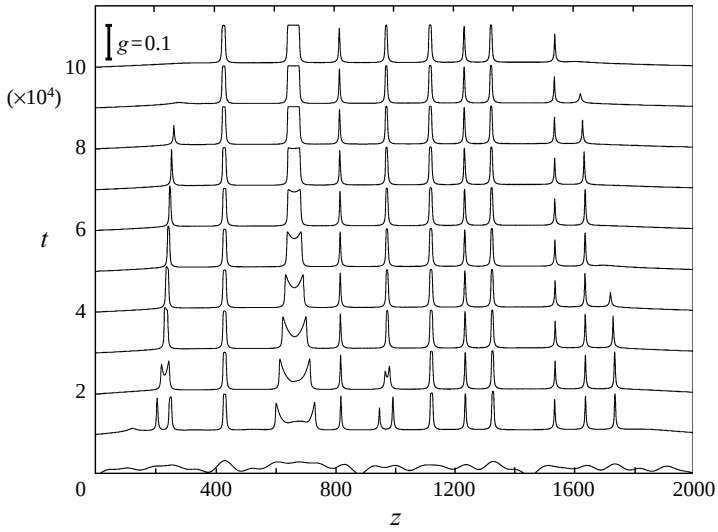

FIGURE 13. Profiles of the buoyancy gradient, g, as a function of z for different values of t in a situation with a different initial condition (shown as the lowest curve). The vertical axis is time, and the profiles are spaced at time intervals of 1 000. As in the previous figure, $r = 50$. The thick bar at the top left-hand corner gives the amplitude scale for g.

The emergence of interfaces from irregularly spaced positions in the domain leads to a less uniform pattern of gradient spikes: those shown in figure 13 have varying thickness.

The third kind of behaviour, in which g_i is to the right of the unstable region in figure 5, is qualitatively different from the layer-forming case. In this regime the large buoyancy gradient in the central region is stable because $\mathscr{F}'(g_i) > 0$, but the edge regions contain unstable buoyancy gradients. In this case, the dynamics of the edge layers is dominant. An example for which the initial value of the gradient in the interior is stable is shown in figure 14: $g_i = 0.06$ and the other parameters are as before. In this case, the shoulder of the edge layer is unstable and 'mixing fronts' rapidly appear there. These features are broader than the gradient spikes in figure 13. Subsequently, the fronts plough into the featureless interior and eventually meet in the middle; ultimately there is a decaying state with a single interface in the middle of the domain (see figure 14).

Further details of the solution are shown in figures 15 and 16. Figure 15 shows a snapshot of g, e and f; note the low kinetic energy density in the strongly stratified interior. Figure 16 shows the snapshot in the (f, g)-plane with the equilibrium flux–gradient relation superposed. The system hugs the equilibrium flux–gradient relation everywhere except in the mixing front which separates the edge from the centre (the connection between points a and b in figure 16).

To our knowledge, the third case, which depends crucially on the ultimate rise of the equilibrium flux–gradient relation (see figure 3), has not been observed in experiments. Hence, an experimental observation of this hypothetical regime would provide support for the hypothesis that the equilibrium flux–gradient relation has the N-shape in figure 3.

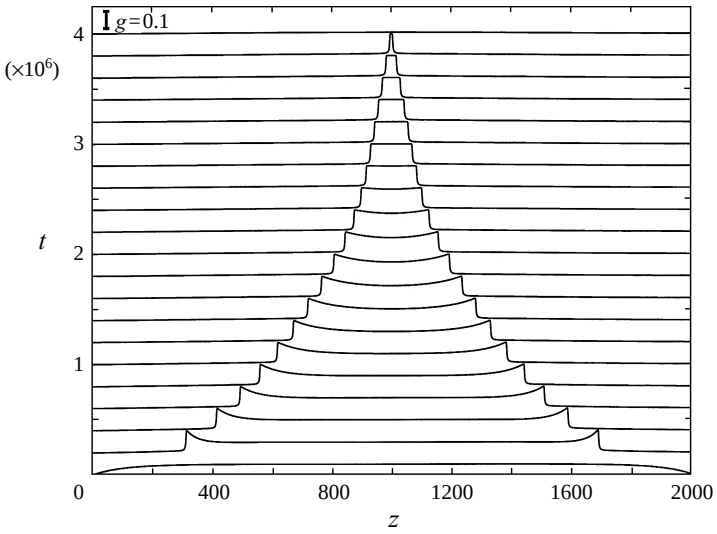

FIGURE 14. Profiles of the buoyancy gradient, g, as a function of z for different values of t in a situation with initial condition $g_i = 0.06$, i.e. to the right of the instability region in figure 5. The vertical axis is time, and the profiles are spaced at time intervals of 1 000; $r = 50$. The thick bar at the top left-hand corner gives the amplitude scale for g.

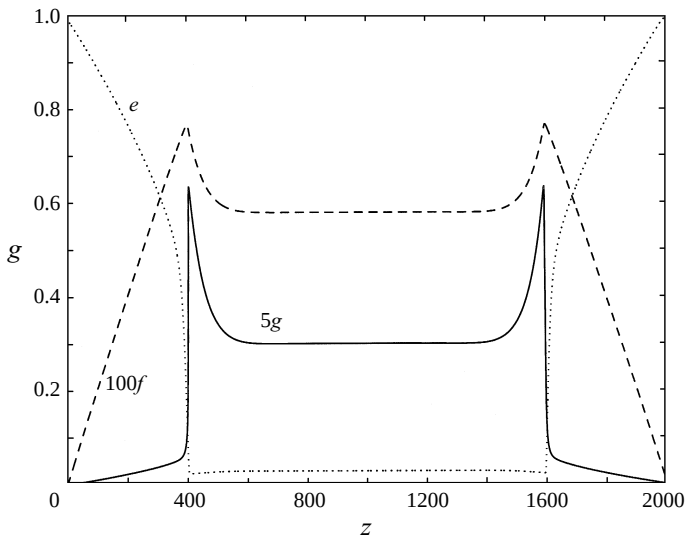

FIGURE 15. Kinetic energy density, e, scaled buoyancy gradient, $5g$, and scaled buoyancy flux $100f$ at $t = 380\,000$. This is a situation where the initial condition is to the right of the unstable region of figure 5.

4.4. *The expansion of the edge layers*

Figures 11 and 14 both show that the advance of the edge layers into the centre is not linear in time. We follow the advance of the edge layers by recording the position $z_*(t)$ for which g is first equal to $2\epsilon/3$. (This choice is not as arbitrary as it first might seem: see § 6.) Figure 17 shows $z_*(t)$ for various values of g_i and ϵ. The data show that $z_* \sim t^{1/2}$, although the destruction of spikes at the boundary of the edge layer

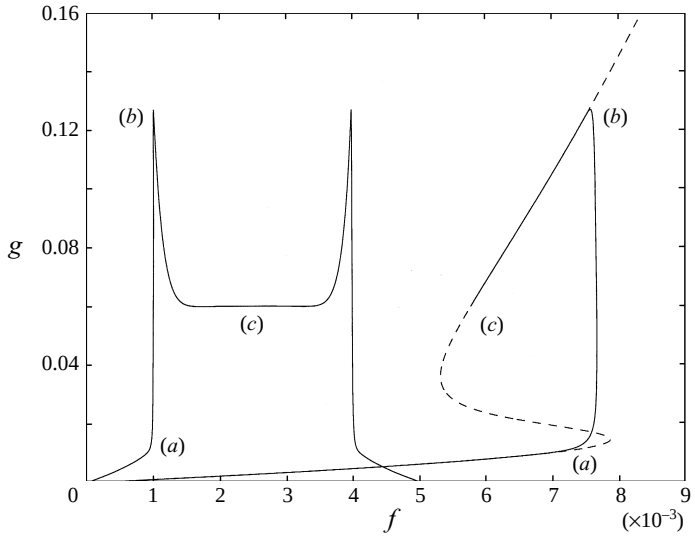

FIGURE 16. The dashed S-shaped curve shows the equilibrium flux-gradient relation in the (f, g) plane. The solid curve, which partially follows the equilibrium relation, is the flux-gradient relation for the numerical solution at $t = 380\,000$. The curve on the left is the buoyancy gradient (plotted on an arbitrary horizontal scale). From the origin to (a), and again from (b) to (c), the numerical solution is on the equilibrium curve. The 'mixing front' is the sharp transition connecting points (a) and (b).

results in variations about the $t^{1/2}$ law for the case in which there is a central layering regime.

The $t^{1/2}$ behaviour motivates a search for similarity solutions in § 6. In anticipation of that development, figures 18 and 19 show the edge solution plotted against the similarity variable $\eta \equiv z/t^{1/2}$. Figure 18 shows the edge solutions for various values of g_i at $\epsilon = 0.02$, and figure 19 shows them for three values of ϵ at fixed g_i. When plotted against η, the solutions at different times condense onto common curves that depend upon the initial buoyancy gradient g_i. These curves, however, are relatively insensitive to the value of ϵ.

4.5. *Parameter variations*

Finally we briefly mention the effect of varying the other parameters of the problem, H and ϵ.

Variations in the size of the domain do not affect the overall features of the solution, such as spike formation, merger and the advance of the edge layers. However, if the domain is too small, the quasi-equilibrium central staircase cannot form because it is eroded away from the sides before a mature pattern of gradient spikes develops. A more quantitative estimate follows from the facts that the edge layer advances at the rate $z_* \sim t^{1/2}$, but the instability grows on a characteristic timescale of order ϵ^{-2} when ϵ is small (this is evident from the results of §3). Hence if $\epsilon^2 H^2 < 4$, patterns do not have time to emerge. For $\epsilon = 0.02$, this implies that spikes appear only if $H > 100$, which is in rough accord with what one might anticipate from the numerical solution in figure 6.

Provided that one stays well above the bottom of the unstable region in figure 5 (i.e. provided that $r > 7 + 4\sqrt{3}$) the qualitative properties of the solution are not

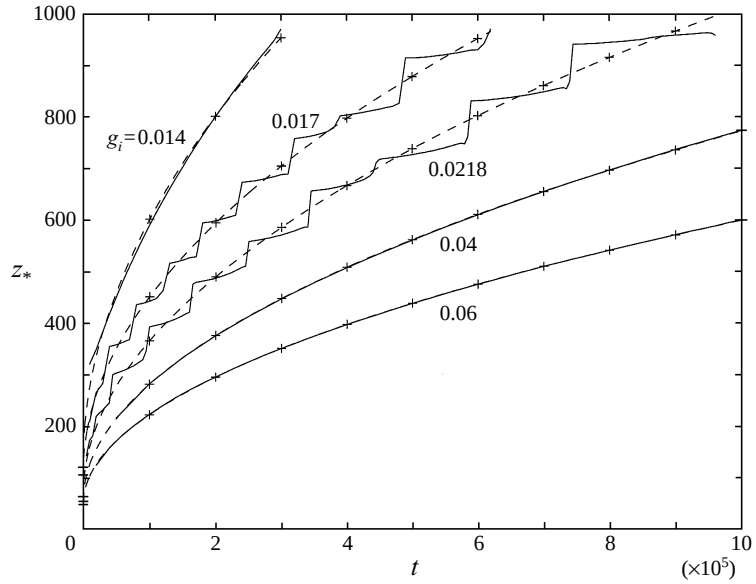

FIGURE 17. The edge layer boundary, $z_*(t)$, (solid curves) against time for several values of g_i; $z_*(t)$ is the location at which g first reaches the value $2\epsilon/3$. The dashed curves and crosses are the best fits to $z_*(t)$ by expressions of the form $at^{1/2} + b$.

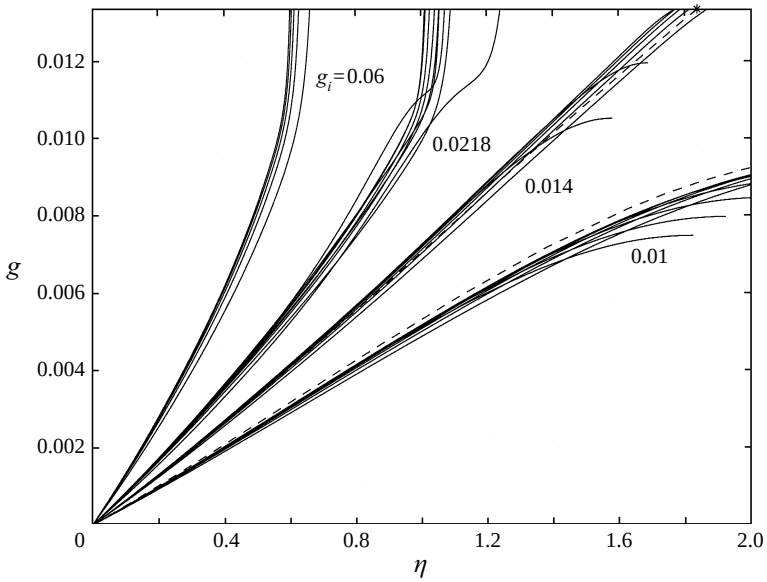

FIGURE 18. The solution in the edge layer plotted against $\eta = z/t^{1/2}$ for different values of g_i with $r = 50$. The dashed lines are similarity solutions constructed in §6.

sensitive to variations in $\epsilon = 1/r$. However, one quantitative consequence of varying ϵ is to change the special flux value, f_*, in the interior of the domain. A summary of numerical calculations showing the variation of f_* with ϵ is displayed in figure 20. Evidently $f_* \propto \epsilon$ for small ϵ.

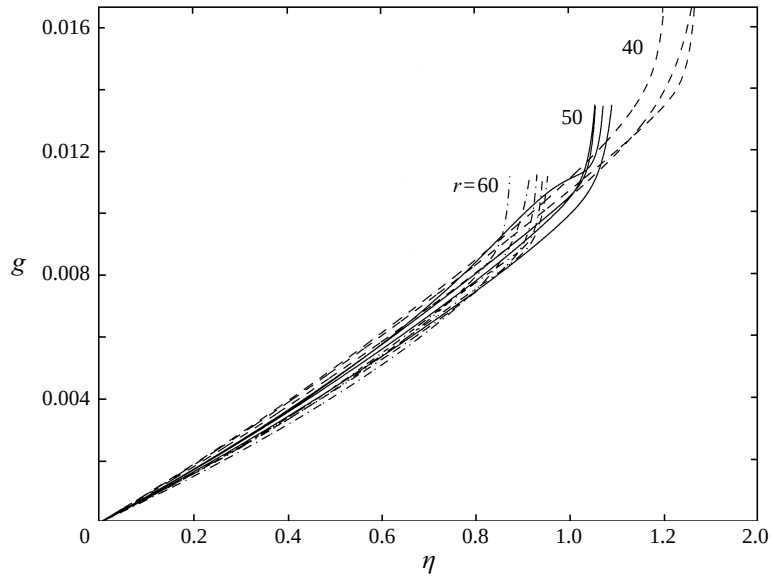

FIGURE 19. Numerical solution in the edge layer plotted against $\eta = z/t^{1/2}$ for three values of ϵ and $g_i = 0.0218$. The edge layer is defined to extend from $z = 0$ to the point $z_*(t)$ where g first reaches the value $2\epsilon/3$.

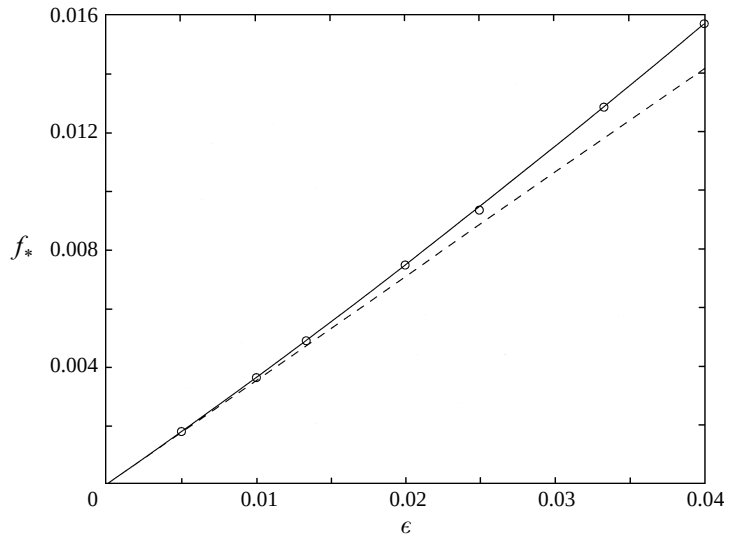

FIGURE 20. The circles are the values of the special flux value f_* found from the numerical solutions plotted against ϵ. The dashed line is $f_* = \epsilon/2\sqrt{2}$. The solid line is obtained from the constant-flux solutions of § 5.

5. Constant-flux solutions

The numerical solutions described in the last section show that over extensive regions, and for significant periods, the system evolves slowly with a nearly uniform buoyancy flux; see figure 8. Motivated by this numerical result, we now construct steady, constant-flux solutions that help us understand the gradient spike patterns in figures 6, 7 and 13.

If the solutions have constant flux, f, then the buoyancy equation (3.3a) is satisfied and we can determine g in terms of e and f from the relation

$$f = \frac{eg}{(e+g)^{1/2}} \qquad \text{or} \qquad g = \frac{2e}{\psi - 1}, \tag{5.1}$$

where

$$\psi \equiv (1 + 4e^3/f^2)^{1/2}. \tag{5.2}$$

For steady solutions, the energy equation (3.3b) can then be written as

$$\beta g^{-1}(g^{-1}e_z)_z + \frac{1-\psi}{2e} + \epsilon f^{-2}e(1-e) = 0. \tag{5.3}$$

If we multiply this equation by e_z and integrate, we find

$$\tfrac{1}{2}\beta(g^{-1}e_z)^2 + U = E, \tag{5.4}$$

where the potential, $U(e)$, is

$$U \equiv -\tfrac{1}{3}\psi - \tfrac{1}{6}\ln\left(\frac{\psi-1}{\psi+1}\right) - \tfrac{1}{2}\ln e + \frac{\epsilon}{f^2}\left(\tfrac{1}{2}e^2 - \tfrac{1}{3}e^3\right), \tag{5.5}$$

and E is a constant of integration.

It is now convenient to use the buoyancy b instead of z as an independent variable. Because

$$g^{-1}\frac{\mathrm{d}}{\mathrm{d}z} = \frac{\mathrm{d}}{\mathrm{d}b}, \tag{5.6}$$

the energy equation (5.4) then becomes

$$\tfrac{1}{2}\beta e_b^2 + U = E. \tag{5.7}$$

Equation (5.7) is the equation of motion of a nonlinear oscillator in which the coordinate b plays the role of time, e is the displacement, U is the potential and β is mass.

The potential $U(e)$ is shown in figure 21. One's attention is immediately drawn to case (b) which shows that if f is selected carefully then the oscillator has a heteroclinic solution connecting the two maxima of the potential, e_{min} and e_{max}: that is, a solution which is a single isolated 'kink' connecting e_{min} to e_{max} (see figure 22a). We denote this special value of the flux by $f_*(\epsilon)$.

Experience with systems like the Cahn–Hilliard equation (Bates & Xun 1995; Kawasaki & Ohta 1982; Fraerman *et al.* 1997) informs us that these special heteroclinic solutions can be used to construct more complicated solutions in which e alternates between e_{max} and e_{min}: see figure 22(b). For instance, one can build a gradient spike solution by superposing a pair of relatively close kinks. These composite solutions are slowly evolving assemblages of kinks: each kink interacts with its immediate neighbours through overlap of exponentially small tails (Balmforth 1995). It is very likely that the coarsening phenomenology of figure 11 springs from these dynamics.

From the heteroclinic solution we obtain e_{min} and e_{max}, and then calculate g_{max} and g_{min} from (5.1) and (5.2). Then, as in figure 12, one has $f_* = \mathscr{F}(g_{min}) = \mathscr{F}(g_{max})$ where $\mathscr{F}(g)$ is the equilibrium flux–gradient relation in (3.2). (Essential to this argument is the observation that e_{max} and e_{min} are equilibrium solutions of the oscillator equation (5.7); these equilibrium solutions are the homogeneous states connected by the kink solution in figure 22.) In figure 21, with $\epsilon = 1/50$, it turns out that $f_* = 0.00747$. For other values of ϵ, the result is shown as the solid curve in figure 20; there is

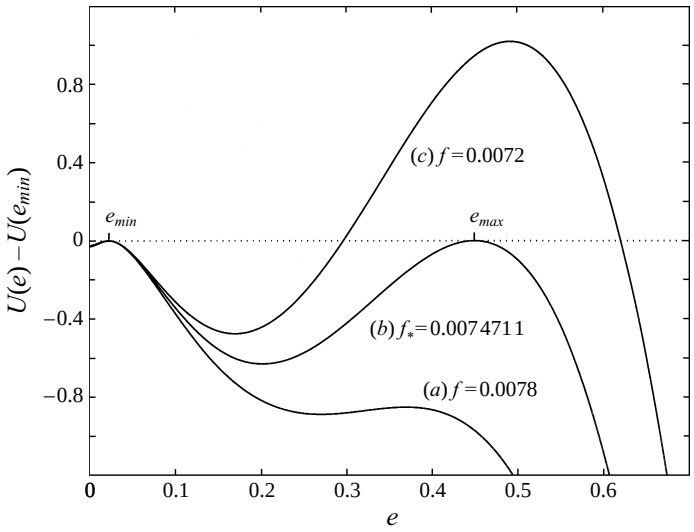

FIGURE 21. The potential U for three different values of f with $\epsilon = 0.02$. In case (b), with $f = f_*$, the two maxima have the same height and so there is an heteroclinic solution.

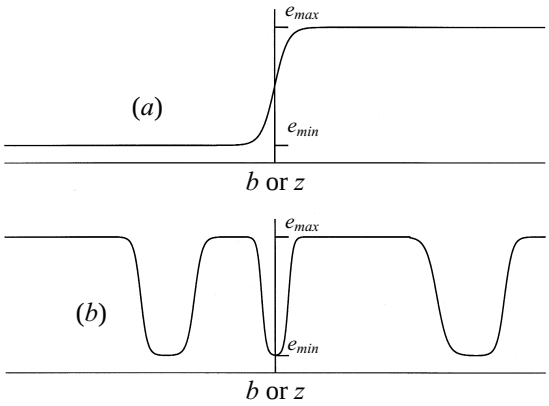

FIGURE 22. (a) A schematic illustration of the kink solution which connects e_{min} and e_{max}; equivalently, g_{max} and g_{min}. (b) A schematic illustration of kink composition.

agreement with the results obtained by measuring the value of the constant flux in the central region of solutions such as that in figure 8. Also shown in figure 20 is the leading-order approximation $f_* = \epsilon/2\sqrt{2} + O(\epsilon^2 \ln \epsilon)$ obtained by working on the oscillator equations (5.5) and (5.7).

6. The edge layer solution

The numerical solutions of §4 show the existence of an 'edge layer'. A typical solution is shown in figure 15; the regions we refer to as 'edge layers' are $0 < z < 400$ and $1\,600 < z < 2\,000$. Figure 15 is a clean example because the large value of g_i in the central domain ($400 < z < 1\,600$) ensures that layers do not form in this region. However it is clear from figure 7 that the edge layer is also a distinctive regime even when the central region exhibits strong layering. Figure 17 suggests that in both cases

the expansion of the edge layer is self-similar with $z_*(t) \sim t^{1/2}$. This motivates us to search for a similarity solution, $g = g(\eta)$ and $e = e(\eta)$, where $\eta = z/t^{1/2}$. Substituting this form into the energy equation (3.3*b*) gives

$$\frac{1}{t}\left[(le^{1/2}e_\eta)_\eta + \tfrac{1}{2}\eta e_\eta\right] = f - \epsilon(e+g)^{1/2}(1-e). \tag{6.1}$$

Evidently, the equations do not completely take similarity form. However, as $t \to \infty$, we neglect the left-hand side of (6.1), and so obtain the following set of ordinary differential equations:

$$f_{\eta\eta} + \tfrac{1}{2}\eta g_\eta = 0, \quad f = \epsilon(e+g)^{1/2}(1-e), \quad f = eg/(e+g)^{1/2}. \tag{6.2a–c}$$

The final two equations are algebraic relations and if we eliminate e we obtain the equilibrium flux–gradient relation, $f = \mathscr{F}(g)$ of figure 3. The inverse function, $g = \mathscr{G}(f)$, is an S-shaped curve in the (f, g)-plane, e.g. see figure 16. Using this multi-valued function we can rewrite (6.2*a–c*) in the suggestive form

$$f_{\eta\eta} + \tfrac{1}{2}\eta \frac{\mathrm{d}\mathscr{G}}{\mathrm{d}f} f_\eta = 0. \tag{6.3}$$

This form emphasizes the singularities which occur at the point where $\mathscr{G}' = \infty$, e.g. near (*a*) in figure 16.

In the edge layer, $g \ll e$, and so (6.2*b–c*) can be simplified to

$$e \approx 1 - \epsilon^{-1}g \qquad \text{and} \qquad f \approx \epsilon(1-G)^{1/2}G. \tag{6.4}$$

Then (6.2*a*) can be written as

$$\left((1-G)^{1/2}G\right)_{\eta\eta} + \tfrac{1}{2}\eta G_\eta = 0, \tag{6.5}$$

where $G \equiv g/\epsilon$. Equivalently,

$$G_{\eta\eta} + \frac{3G-4}{2(2-3G)(1-G)}G_\eta^2 + \eta\frac{(1-G)^{1/2}}{2-3G}G_\eta = 0. \tag{6.6}$$

Equation (6.6) has singular points at $G = 2/3$ and $G = 1$. The first of these, $G = 2/3$, is the $g \ll 1$ approximation to the first turning point of the flux–gradient relation in figure 16: see equation (6.3). The second, $G = 1$, is an artifact of the approximation $e \gg g$. (In fact, there is another singularity but, as (6.3) shows, it is at the second turning point of the flux–gradient relation.)

To solve the similarity equation (6.6) we need to apply boundary conditions. However, this is not straightforward, and we need to introduce some simplifications. The intention is to model an expanding edge layer. Provided the domain is sufficiently large, we may consider just one of the edge layers in isolation: we consider the lower edge layer for illustration. Then one boundary condition is the no-flux requirement, $G(0) = 0$.

The second boundary condition is more delicate. For simplicity we assume that the domain is sufficiently wide to apply a condition as $\eta \to \infty$. The form of the initial condition suggests we take $G(\infty) = G_i$, corresponding to $g = g_i$ in the interior.

Solutions to the boundary value problem (6.6) with $G(0) = 0$ and $G(\infty) = G_i$ are shown in figure 23. These solutions exist provided $G_i < 2/3$. This condition is equivalent to the requirement that the point (g_i, r) lies to the left of the solid curve in figure 5: that is, the initial gradient in the central region is stable and layers do not form.

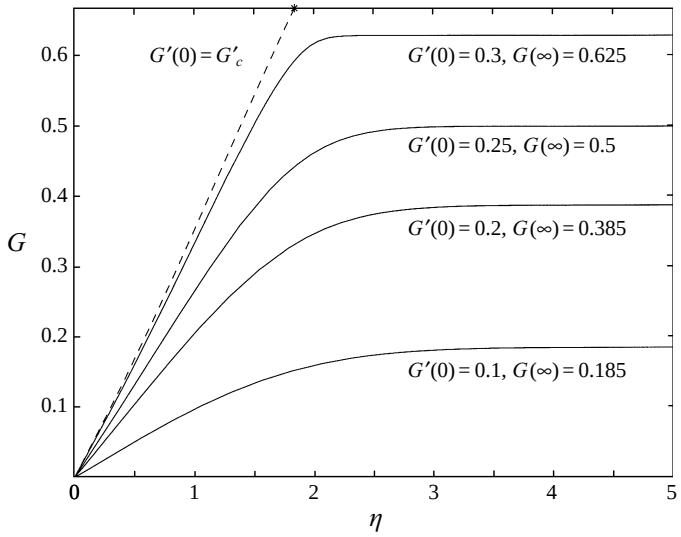

FIGURE 23. Similarity solutions for various values of $G(\infty)$, or equivalently, $G'(0)$. As $G_i \to 2/3$, the family of similarity solutions limits to a function that reaches $G = 2/3$ at $\eta = \eta_s \approx 1.837$ (the dashed curve, for which $G'(0) = G'_c \approx 0.354$). Thereafter, with $\eta > \eta_s$, $G = 2/3$. In the limit, the function has a discontinuous gradient at $\eta = \eta_s$.

The similarity solutions take the form of monotonically increasing functions over the interval. In fact, when $G_i \ll 1$, one can linearize (6.6) and this similarity solution is the well known 'erf' characteristic of linear diffusion.

For $G_i = 2/3$, there is a limiting solution that reaches $G = 2/3$ at $\eta = \eta_s \approx 1.837$, and then is flat (i.e. $G = 2/3$ for $\eta > \eta_s$): that is, a function with discontinuous gradient (this solution is drawn as the dashed line in figure 23). The limiting case corresponds to the marginal stability of the central region. For $G_i > 2/3$, there are no regular solutions of the boundary value problem, and the central region is either unstable, or there is an instability in the edge layer itself. In other words, the non-existence of the similarity solution is implicitly connected to instability.

In the stable case, we therefore expect that the edge layers expand self-similarly. Indeed, the similarity solution shows agreement with the edge layer solutions of the full equation: the curves labelled $g_i = 0.01$ and $g_i = 0.014$ in figure 18 show numerical solutions for the stable case; the nearby dashed lines denote the similarity solutions.

When the initial gradients are unstable in either the central region or the edge layer however, there are no similarity solutions. Nevertheless, figure 18 indicates that the numerical solution of the full equations still takes something close to similarity form in the edge layer, even though $G_i > 2/3$.

In the case in which the central region is unstable, and layers form in the interior, the similarity scaling $z \sim t^{1/2}$ can only be interpreted as an average of the saltatory advance of the edge layers: the curves labelled 0.017 and 0.0218 in figure 17 show sudden jumps in z_* as gradient spikes are eroded from the periphery of the spike pattern. (Note that, in figures 17 and 18, we located the boundary of the edge layer according to the criterion $g = 2\epsilon/3$; for $\epsilon \ll 1$, this is the singular point where the similarity scaling must break down.)

When the centre does not layer, the numerical solution shows a cleaner self-similar scaling. In fact, the solution in the interior also takes a similarity form. However, the similarity scaling breaks down at the mixing front separating the edge layer and

interior (figure 15). A simple analytical characterization of this structure has eluded us.

Finally, the similarity equation (6.6) is independent of ϵ. This property also approximately extends to the numerical solutions of the full equations: figure 19 shows that the form of the edge layer solution is roughly independent of ϵ for fixed initial gradients.

7. Discussion

In this paper we have crudely modelled the evolution of a turbulent and stratified fluid. Solutions of the model equations display features such as the relatively rapid formation of mixed layers separated by interfaces, the subsequent slower development of the pattern of interfaces, and the ultimate decay to the homogeneous state. The slow development of the pattern takes place through layer merger in the interior, and by the advance of the edge layers. The pattern itself is characterized by a nearly constant buoyancy flux, with any residual variations stemming from layer merger events. These aspects of the model are in agreement with the experiments of Ruddick *et al.* (1989) and Park *et al.* (1994).

In addition to layering, the model also predicts two other types of evolutionary behaviour. First, when the initial state is not sufficiently strongly stratified, or if the turbulence is sufficiently intense, turbulent mixing is unimpeded by the stable stratification and the system decays to the homogeneous state without forming layers and interfaces. This too is a prominent feature of the experiments.

If the initial stratification is very strong, then layering is suppressed in the interior and only in the edge regions is there an instability. Mixing fronts form in each edge layer and then erode into the stable interior. This type of evolution has not been seen in experiments. However, it is not clear whether those experiments have been carried out at sufficiently high Richardson numbers to isolate this hypothetical regime; this is a testable prediction of our model.

The model also predicts several other features of the system, some of the more notable ones being the following:

(*a*) The edge layers advance at a rate $t^{1/2}$. Moreover the solution is nearly self-similar.

(*b*) Layer merger events continue indefinitely. As time proceeds though, and the mixed layers cover larger and larger areas, the timescale for merging becomes exponentially long. This type of behaviour is expected from asymptotic theory of coherent structure interactions (reviewed by Balmforth 1995), and from the analogy with Cahn–Hilliard dynamics.

(*c*) Gradient spikes have a maximum amplitude dictated by the upper branch of the flux–gradient relation. However, depending on how many times the layers have merged, their thickness can vary greatly. In experimental terms, this means that interfaces may have different thicknesses, but the interfacial buoyancy gradient does have a maximum value.

(*d*) The initial pattern of gradient spikes emerges as a result of linear instability. Consequently, simple initial states such as (4.1*a, b*) or those used in the experiments show that the spike pattern appears first at the edges, then works into the interior. However, by preparing experiments with different initial conditions it should be possible to produce patterns that emerge first in the centre of the domain (cf. figure 13).

(*e*) Edge layers appear because of the no-flux boundary conditions. If, however,

we maintain a constant flux near the special value, f_*, then the edge layers do not appear. Instead, the pattern of gradient spikes occupy the whole domain and coarsening continues until the pattern reaches a final state with a single, thick interface (we have computationally verified this).

These features of the model are all potentially testable by existing or new experiments. For example, the $t^{1/2}$ advance of the edge layers might be verified by existing experimental data.

Another test of the theory is to change the way the experiment is performed. Our model relies upon the idea that the stirrer operates at fixed speed. Importantly, this is different to delivering either constant force or power. Modified experiments using these alternative forcing mechanisms may be feasible.

One basic flaw of the model is that it describes the turbulent fluid in terms of horizontally averaged kinetic energy density and buoyancy. This cannot adequately represent the details of turbulence. All of these details are swept conveniently into the 'universal constant' ϵ.

Perhaps one way to represent more of the turbulent dynamics is by including 'fluctuations', as well as the averages, much as one follows standard averaging or mean field methods. Most crudely one might try to model the fluctuations as a random forcing of the mean equations. In fact, such forcings, even if very small, can play an important role in the layer dynamics, since the layer interactions are exponentially weak for thick layers and hence prone to being overshadowed by random noise. In that circumstance, one expects the layer merging to cease at some stage, and random drifting of the gradient spikes to ensue, much like a Brownian motion (see Kawakatsu & Munakata 1985).

In any event, the model is not intended to be a quantitative theory of the dynamics of stratified, turbulent fluid. At best it establishes a language of inquiry that may guide future experimental and theoretical directions. Moreover, once we have some grounds for believing the model results, we may hope to adapt it to problems in astrophysical and geophysical fluid dynamics.

This work began at the 1996 Woods Hole Oceanographic Institution's Summer Study Program on Geophysical Fluid Dynamics. We thank the Director, Steve Meacham, and all the participants for a productive summer; it is a pleasure to recall summer conversations on stratified layering with Barry Ruddick. This research was supported by the National Science Foundation under award OCE-9616017 with additional support for N.J.B. from the Green Foundation and for S.G.L.S. by a Lindemann Trust Fellowship.

Appendix. Amplitude expansion near the critical point

The dynamics revealed by numerical simulation is characteristic of gradient systems familiar in theory of phase transitions. We can go further in drawing this analogy by deriving an amplitude equation valid in one asymptotic limit of the model equations. This amplitude equation is the Cahn–Hilliard equation, a classical system used in phase transition theory (Cahn & Hilliard 1958).

The critical point is at

$$r_0 = 7 + 4\sqrt{3}, \quad g_0 = -\frac{1}{2} + \frac{1}{\sqrt{3}}, \quad e_0 = \frac{1}{2} - \frac{1}{2\sqrt{3}}. \tag{A 1}$$

We then expand r, g and e about their critical values:

$$r = r_0 + \epsilon^2 r_2 + \cdots, \quad g = g_0 + \epsilon g_1 + \cdots, \quad e = e_0 + \epsilon e_1 + \cdots. \tag{A 2}$$

Note that we expand such that the energy and buoyancy perturbations scale like ϵ, while the criticality parameter is $O(\epsilon^2)$. To complete the asymptotic reduction of the problem we further need to rescale the space and time coordinates. The appropriate time and spatial scales are given by $T = \epsilon^4 t$ and $Z = \epsilon z$.

Given the series (A 2), and the long length and time scales, we may then rewrite the governing equations, order the various terms according to powers of ϵ, and solve order by order. The leading orders give algebraic relations:

$$g = g_0 + [g_1 + A(Z,T)]\epsilon + \left[(9+6\sqrt{3})(g_1 + A(Z,T))^2 - \frac{33-19\sqrt{3}}{12} r_2\right]\epsilon^2 + O(\epsilon^3), \tag{A 3a}$$

$$e = e_0 - (2+\sqrt{3})[g_1 + A(Z,T)]\epsilon + O(\epsilon^3), \tag{A 3b}$$

$$r = r_0 + r_2\epsilon^2 + O(\epsilon^3). \tag{A 3c}$$

Note that, according to (A 3*a*), there is a redundancy in g_1 and the vertical average of the perturbation amplitude $A(Z,T)$; we remove this ambiguity by defining $A(Z,T)$ to have zero spatial average. At order ϵ^5, we need to apply a solvability condition which gives an equation for the amplitude function A. This governing equation is the Cahn–Hilliard equation:

$$A_T = \frac{\partial^2}{\partial Z^2}\left\{\left[2^{1/2}3^{5/4}(9+5\sqrt{3})g_1^2 - 2^{-5/2}3^{1/4}(-19+11\sqrt{3})r_2\right]A - 2^{-3/2}3^{1/4}(2+\sqrt{3})A_{ZZ} + 2^{1/2}3^{5/4}(9+5\sqrt{3})A^2 + 2^{1/2}3^{1/4}(9+5\sqrt{3})A^3\right\} \tag{A 4}$$

$$\approx [(98.6g_1^2 - 0.012r_2)A - 1.74A_{ZZ} + 98.6g_1A^2 + 32.9A^3]_{ZZ}. \tag{A 5}$$

The formation of layers and their subsequent slow evolution and merging is a well known feature of Cahn–Hilliard dynamics (Cahn & Hilliard 1958; Bates & Xun 1995). In fact, the motion of layers in the Cahn–Hilliard system is strikingly similar to the world lines of the gradient spikes shown in figure 11 (Kawasaki & Ohta 1982; Kawakatsu & Munakata 1985).

REFERENCES

Balmforth, N. J. 1995 Solitary waves and homoclinic orbits. *Ann. Rev. Fluid Mech.* **27**, 335–373.

Barenblatt, G. I. 1983 Selfsimilar turbulence propagation from an instantaneous plane source. In *Nonlinear Dynamics and Turbulence* (ed. G. I. Barenblatt, G. Iooss & D. D. Joseph). Interaction of Mechanics and Mathematics Series, chap. 3, pp. 48–60. Pitman.

Barenblatt, G. I., Bertsch, M., Dal Passo, R., Prostokishin, V. M. & Ughi, M. 1993 A mathematical model of turbulent heat and mass transfer in stably stratified shear flow. *J. Fluid Mech.* **253**, 341–358.

Bates, P. W. & Xun, J. P. 1995 Metastable patterns for the Cahn–Hilliard equation. 2. Layer dynamics and slow invariant manifolds. *J. Diff. Equat.* **117**, 165–216.

Browand, F. K., Guyomar, D. & Yoon, S.-C. 1987 The behaviour of a turbulent front in a stratified fluid with an oscillating grid. *J. Geophys. Res.* **92**, 5329–5341.

Cahn, J. W. & Hilliard, J. E. 1958 Free energy of a nonuniform system. I. Interfacial free energy. *J. Chem. Phys.* **28**, 258–267.

Chen, C. F. & Turner, J. S. 1980 Crystallization in a double-diffusive system. *J. Geophys. Res.* **85**, 2573–2593.

Fincham, A. M., Maxworthy, T. & Spedding, G. R. 1996 Energy dissipation and vortex structure in freely decaying stratified grid turbulence. *Dyn. Atmos. Oceans* **23**, 155–169.

Fraerman, A. A., Mel'nikov, A. S., Nefedev, I. M., Shereshevskii, I. A. & Shpiro, A. V. 1997 Nonlinear relaxation dynamics in decomposing alloys: One-dimensional Cahn–Hilliard model. *Phys. Rev.* B **55**, 6316–6323.

Holford, J. M. & Linden, P. F. 1997*a* Boundary-driven layering in a turbulent stratified flow. Submitted to *Phys. Fluids.*

Holford, J. M. & Linden, P. F. 1997*b* The development of layers in a stratified fluid. In *Proc. 5th IMA Conf. on Stratified Flows*. Oxford University Press. In press.

Ivey, G. N. & Corcos, G. M. 1982 Boundary mixing in a stratified fluid. *J. Fluid Mech.* **121**, 1–26.

Kawakatsu, T. & Munakata, T. 1985 Kink dynamics in a one-dimensional conserved TGDL system. *Prog. Theor. Phys.* **74**, 11–19.

Kawasaki, K. & Ohta, T. 1982 Kink dynamics in one-dimensional nonlinear systems. *Physica* **116A**, 573–593.

Keast, P. & Muir, P. 1991 Algorithm 688 – EPDCOL – a more efficient PDECOL code. *ACM Trans. Math. Software* **17**, 153–166.

Linden, P. F. 1979 Mixing in stratified fluids. *Geophys. Astrophys. Fluid Dyn.* **13**, 3–23.

Park, Y.-G., Whitehead, J. A. & Gnanadeskian, A. 1994 Turbulent mixing in stratified fluids: layer formation and energetics. *J. Fluid Mech.* **279**, 279–311.

Phillips, O. M. 1972 Turbulence in a strongly stratified fluid—is it unstable? *Deep-Sea Res.* **19**, 79–81.

Posmentier, E. S. 1977 The generation of salinity finestructure by vertical diffusion. *J. Phys. Oceanogr.* **7**, 298–300.

Rehmann, C. R. & Koseff, J. R. 1997 Mean potential energy change in weakly and strongly stratified grid turbulence. Submitted to *J. Fluid Mech.*

Ruddick, B. R., McDougall, T. J. & Turner, J. S. 1989 The formation of layers in a uniformly stirred density gradient. *Deep-Sea Res.* **36**, 597–609.

Schmitt, R. W. 1994 Double diffusion in oceanography. *Ann. Rev. Fluid Mech.* **26**, 255–285.

Spiegel, E. A. 1969 Semiconvection. *Commun. Astrophys. Space Phys.* **1**, 57–61.

Thorpe, S. A. 1982 On the layer produced by rapidly oscillating a vertical grid in a uniformly stratified fluid. *J. Fluid Mech.* **124**, 391–409.

Turner, J. S. 1973 *Buoyancy Effects in Fluids*, 1st edn. Cambridge University Press.

Turner, J. S. 1985 Multicomponent convection. *Ann. Rev. Fluid Mech.* **17**, 11–44.